Assessing the viability of Caesium-based double perovskite for technological applications

H. Mansour[a,b] and D. Rached[b]

[a]*Department of Physics, Faculty of Sciences, Blida University, P.O. Box 270, Route de Soumaa, Blida, 09000, Algeria.*
[b]*Magnetic Materials Laboratory (MML), Faculty of exact sciences, Djillali Liabes University of Sidi Bel-Abbes, Sidi Bel-Abbes, 22000, Algeria.*

Received 27 July 2024; accepted 7 June 2025

This research aims to provide a comprehensive understanding of the structural, elastic, electronic, and optical properties of the $Cs_2PbBeBr_6$ halide double perovskite (HDP). In this study, all self-consistent field (SCF) calculations were performed using density functional theory (DFT) within the full-potential linear augmented plane-wave (FP-LAPW) method, as implemented in the Wien2k code. The Perdew-Burke-Ernzerhof (PBE) generalized gradient approximation (GGA) and the Tran-Blaha modified Becke−Johnson (TB-mBJ) methods were employed to accurately describe the exchange-correlation interactions. Our findings indicate that $Cs_2PbBeBr_6$ is stable in a cubic structure (Fm-3m), supported by phase stability analysis, enthalpy of formation, tolerance factor, and elastic constants. The compound exhibits ductile behavior, as assessed by Poisson's and Pugh's ratios. The electronic band structure reveals an indirect band gap of 2.243 eV and 3.248 eV, calculated using the GGA and TB-mBJ methods, respectively. Optical spectra calculations were performed in the energy range of 0 to 13 eV for each of the dielectric functions, extinction coefficient, electron energy loss, refractive index, optical conductivity, reflectivity, and absorption coefficient. The optical properties of $Cs_2PbBeBr_6$ in the visible range are particularly significant, offering strong potential for applications such as solar energy harvesting. These characteristics make the compound a promising candidate for optoelectronic devices.

Keywords: GGA and TB-mBJ; halide double perovskite; solar energy; semiconductor.

DOI: https://doi.org/10.31349/RevMexFis.71.060503

1. Introduction

In recent years, the excessive consumption of fossil fuels has led to significant environmental pollution. Therefore, renewable energy sources have gained considerable global attention due to their abundance and safety, such as solar energy, which is largely attributable to their accessibility. Given its widespread accessibility and minimal negative environmental impact, solar energy has emerged as a prominent source of green energy. New technologies and growing concerns about pollution emphasize the need for governments to seek alternative energy sources such as double perovskites to replace the use of oil, gasoline, coal and other fossil fuels [1]. The remarkable capabilities of double perovskites, arising from their diverse structural composition, render them ideal [2,4]. In recent years, extensive research has been conducted on these materials for their applications in photovoltaics, photoluminescence, and thermoelectrics [5-14]. Halide double perovskites (HDPs) typically have the general formula A2BB0X6 , where B and B0 represent transition metals (although not exclusively), A denotes any alkali or alkaline earth metal, and X represents any halogen element [15,16]. Moreover, HDP materials have been extensively studied and have garnered significant attention from researchers due to their applications in fields such as thermoelectrics [17-19], photocatalysis, and optoelectronics [20,21]. HDPs exhibit exceptional stability, a wide range of potential compositions, and attractive optoelectronic properties [22]. However, despite extensive research on innovative HDPs, the power conversion efficiency (PCE) of state-of-the-art double perovskite solar cells (PSCs) still falls short compared to that of dominant lead-based devices [23]. The lasting popularity of halide-based double perovskites can be attributed to their exceptional physical properties, including suitable and tunable bandgaps, high optical absorption coefficients, long diffusion lengths, low effective charge carrier masses, compositional flexibility, and high defect tolerance [24-27]. Several studies have explored the potential optoelectronic applications and thermoelectric features of Cs-based HDPs for multiple compositions such as Cs_2XYI_6 (XY: BeSr, BeCa, GeMg, GeCd, GeBe) [28], $Cs_2A0A00Br_6$ (A0A00 : CdBe, BeMg, CdGe, GeZn, GeMg, MgZn) [29], Cs_2AGeCl_6 (A: Zn, Cd) [22], Cs_2XGeF_6(X: Sn, Pb) [30], Cs_2CuIrF_6 [31], $Cs_2CdZnCl_6$ [32], Cs_2CuBiX_6(X: I, Br, Cl) [33], and Cs_2InBiX_6(X: F, Cl, Br, I) [34]. The motivation for this work stems from the potential of $Cs_2PbBeBr_6$ HDP for diverse applications across various fields of technology. Moreover, the absence of theoretical or experimental studies on these properties highlights the importance of a comprehensive investigation of the $Cs_2PbBeBr_6$ HDP. In this work, we employed first-principles exploration to investigate the structural, elastic, electronic, and optical characteristics of the novel $Cs_2PbBeBr_6$ HDP. Our calculations indicate that the $Cs_2PbBeBr_6$ HDP show promising potential for use in photovoltaic devices due to their stability and exceptional optical properties. These findings will enhance the understanding of the physical characteristics of $Cs_2PbBeBr_6$ HDP and support progress in the experimental synthesis of this compound for solar energy harvesting.

2. Calculation methodology

The calculations are conducted employing the linearized and augmented plane wave technique (FP-LAPW), executed through the Wien2k code [35]. To handle the exchangecorrelation potential, the generalized gradient approximation suggested by Perdew, Burke, and Ernzerhof (GGA-PBE) [36] and the Tran-Blaha modified Becke-Johnson (TB-mBJ) methods [37] were employed. The basis set extension was determined using the criteria $R_{MT} x K_{\max} = 7$, where RMT represents the smallest radius of the muffin-tin, and $K_{\max}$ represents the maximum value of the k-vector in reciprocal space. We set the parameters $G_{\max}$ and $l_{\max}$ (angular momentum vector) to 12 $\text{Ry}^{1/2}$ and 10, respectively. The RMT values used for Cs, Pb, Be, and Br were 2.50, 2.50, 2.32, and 2.50 atomic units, respectively. Computations were performed using a dense mesh of 1000 k-points in the Brillouin zone (BZ). Additionally, we used 3000 k-points for calculating elastic properties ensuring that the elastic constants varied by less than 0.5% as the grid density increased, 2000 k-points for electronic properties, and 4000 k-points for optical properties to ensure accurate computations of these specific properties. Electronic iterations continued until the energy variation between two consecutive iterations was less than 10^{-4} Ry. We performed k-point convergence tests by incrementally increasing the grid density until the relative error between consecutive k-point increases was below 0.2%. For the calculation of the elastic constants, the forces in the SCF (selfconsistent field) cycles were converged to a value of 0.0001 eV/Å.

3. Results and discussion

The following sections discuss the structural, elastic, electronic, and optical properties of the Cs_2PbBeBr6 HDP.

3.1. The structural properties

Optimizing the unit cell geometry defines the structural properties of the $Cs_2PbBeBr_6$ HDP. Figure 1 shows the optimized structural configurations of the $Cs_2PbBeBr_6$ compound. The stoichiometric formula for the studied double perovskite combinations was $Cs_2PbBeBr_6$ HDP, which crystallize in the space group $Fm-\bar{3}m$(# 225). This formula consists of four elements: Cs, Pb, Be, and Br, arranged at a ratio of 2:1:1:6. In this crystal structure, the atomic positions of the Cs atoms are at (0.25, 0.25, 0.25) and (0.75, 0.75, 0.75) at interstitial sites, with Pb, Be, and Br positioned at the (0, 0, 0), (0.5, 0.5, 0.5), and (xBr, 0, 0) sites, respectively. The computed lattice constant was 11.307 Å (Table I).

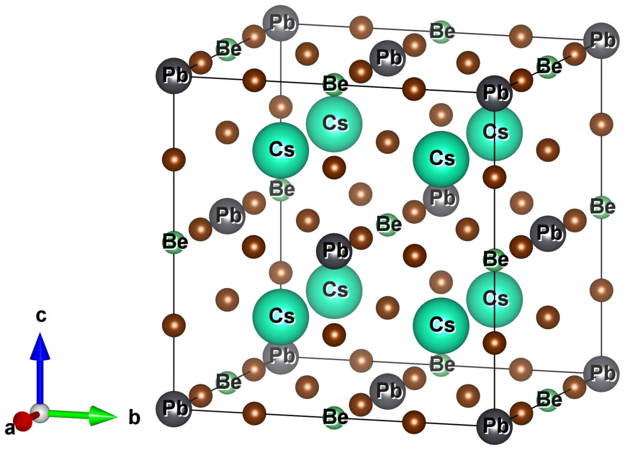

FIGURE 1. Crystal structure of the Cs_2PbBeBr6 HDP.

TABLE I. The lattice constant (a, in Å), bulk modulus (B, in GPa), first derivative of the bulk modulus (B0) , tolerance factor (τ), x-coordinate (x_{Br}) of the Br atom, and enthalpy of formation per formula unit (ΔH_f, in Ry) of the $Cs_2PbBeBr_6$ HDP.

HDP	a(Å)	B(GPa)	B'	τ	x_{Br}	$\Delta H_f(Ry)$
$Cs_2PbBeBr_6$	11.307	22.366	4.856	0.923	0.273	-2.672

Furthermore, the $Cs_2PbBeBr_6$ HDP exhibit very low ground state energy, leading to a stable structure. Optimization curves for the ground state energy are used to determine the optimum parameters that minimize the total energy of a system in its lowest energy state. Figure 2 shows the corresponding volume optimization graph. The optimization curve demonstrated the structural stability of $Cs_2PbBeBr_6$. The optimized lattice parameter, bulk modulus B and its derivative B', ground state energy E_0, and volume at ground state V_0 are obtained using the Murnaghanequation of state [38]:

$$E_{Total} = E_0 + \frac{BV_0}{B'}(B'-1) \times \left(\left[\frac{1-V_0}{V}\right] B + \left[\frac{V_0}{V}\right]^{B'} - 1 \right). \quad (1)$$

Table I presents the obtained values of the structural parameters for the $Cs_2PbBeBr_6$HDP. Additionally, the phase

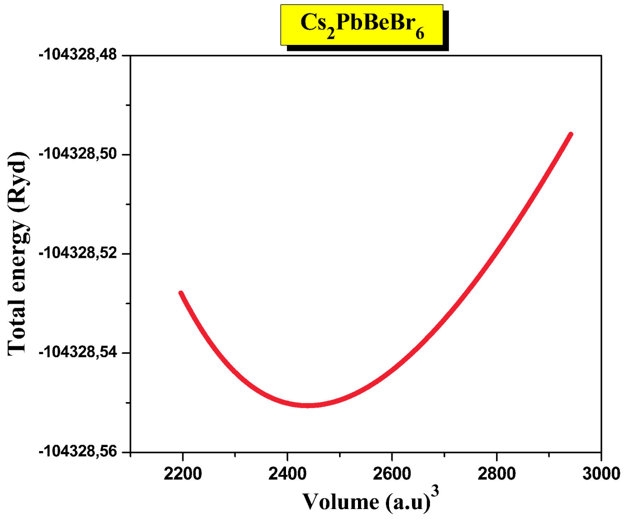

FIGURE 2. Energy as a function of volume for the $Cs_2PbBeBr_6$ HDP.

stability of this HDP structure was assessed using the tolerance factor (τ). The equation used to compute τ is [39]:

$$\tau = \frac{R_{Cs} + R_{Br}}{\sqrt{2}\left(\frac{R_{pb}+R_{Be}}{2} + R_{Br}\right)}. \tag{2}$$

Here, the symbols R_{Cs}, R_{Pb}, R_{Be}, and R_{Br} represent the ionic radii of Cs, Pb, Be, and Br, respectively. For cubic structures, the acceptable values for the tolerance factor fall within the range of $0.9 < \tau < 1.0$ [40,41]. Additionally, we used the following equation to calculate the enthalpy of formation (ΔH_f) to verify the feasibility of synthesizing HDP:

$$\begin{aligned}\Delta H_f &= E_{\text{Tot}}(\text{Cs}_2\text{Pb Be Br}_6) \\ &\quad - [2E_{\text{Cs}} + E_{\text{pb}} + E_{\text{Be}} + 6E_{\text{Br}}],\end{aligned} \tag{3}$$

where E_{Total}($Cs_2PbBeBr_6$) represents the total energy per unit cell of the bulk $Cs_2PbBeBr_6$ HDP, and E(Cs), E(Pb), E(Be), and E(Br) represent the total energy per Cs, Pb, Be, and Br, respectively, in their pure solid state. Table I presents the computed ΔH_f for the $Cs_2PbBeBr_6$ HDP, demonstrating their thermal stability. Additionally, the negative value of ΔH_f indicates that $Cs_2PbBeBr_6$ HDP can be synthesized experimentally.

3.2. Elastic properties

The elastic constants are fundamental physical parameters that characterize the forces exerted on a solid. They play a crucial role in analyzing the mechanical stability of crystal structures. For the cubic crystals under investigation, the three elastic constants C_{11}, C_{12}, and C_{44} are sufficient to elucidate the mechanical stability and related properties of the material [42]. The elastic constants can be easily determined using the IRelast package, which is seamlessly integrated into Wien2k software [43]. The IRelast package uses a stress-strain method to calculate elastic constants. This approach involves applying small deformations to the crystal structure and calculating the corresponding stress tensor for each deformation. The elastic constants are determined by fitting the relationship between stress and strain, based on Hooke's law. The package ensures that various types of deformations, such as shear and tensile, are applied to account for all independent elastic constants according to the symmetry of the crystal. To ensure the stability of mechanical structures, the elastic constants must satisfy the Born-Huang stability criteria [44], which are given as follows:

$$\begin{aligned}&C_{11} - C_{12} > 0, \quad C_{11} + 2C_{12} > 0, \\ &C_{11} > B > C_{12}, \quad C_{44} > 0, \quad \text{and} \quad C_{11} > 0.\end{aligned} \tag{4}$$

The elastic constant values for the $Cs_2PbBeBr_6$ HDP are presented in Table II. The results indicate that the $Cs_2PbBeBr_6$ HDP satisfy the stability requirements, suggesting that the crystal structure of the $Cs_2PbBeBr_6$ is stable.

TABLE II. The calculated elastic constants (C_{ij}), Cauchy pressure (C_p), bulk modulus (B), Shear modulus (G), Young's modulus (Y) all in GPa, Pugh's ratio (B/G), Poisson's ratio (υ), anisotropy constant (A) and melting temperature (T_m, in K) of $Cs_2PbBeBr_6$ HDP.

HDP	$Cs_2PbBeBr_6$
C_{11} (GPa)	40.147
C_{12} (GPa)	10.550
C_{44} (GPa)	13.420
C_p (GPa)	2.869
B (GPa)	22.328
G (GPa)	11.598
Y (GPa)	29.658
B/G	2.925
υ	0.278
A	0.790
T_m (K)	790.266 ± 300

Additionally, to investigate the hardness of the $Cs_2PbBeBr_6$ HDP, key mechanical parameters, including the Cauchy pressure C_p, Bulk modulus B, Shear modulus G, Young's modulus Y all in GPa, Pugh's ratio B/G, Poisson's ratio (υ), anisotropy constant A are considered. These parameters were determined by the following equations:

$$B = \frac{1}{6}(\text{C}_{11} + 2\text{C}_{12}). \tag{5}$$

The Cauchy pressure [45] is defined as

$$\text{C}_p = \text{C}_{12} - \text{C}_{44}. \tag{6}$$

The Voigt G_V and Reuss G_R shear moduli are obtained by [46,47]

$$G_V = \frac{\text{C}_{11} - \text{C}_{12} + 3\text{C}_{44}}{5}, \tag{7}$$

$$G_R = \frac{5(\text{C}_{11} - \text{C}_{12})\text{C}_{44}}{4\text{C}_{44} + 3(\text{C}_{11} - \text{C}_{12})}. \tag{8}$$

The G of cubic crystals can be obtained from Navier's equation [48]

$$G = \frac{(G_v + G_R)}{2}. \tag{9}$$

Poisson's ratio υ [49]

$$\upsilon = \frac{3B - 2G}{2(3B + G)}. \tag{10}$$

Young's modulus Y [50]

$$Y = \frac{9BG}{3B + G} \tag{11}$$

The Zener anisotropy factor A [51,52]

$$A = \frac{2\text{C}_{44}}{(\text{C}_{11} - \text{C}_{12})}. \tag{12}$$

Typically, the shear modulus G represents a material's resistance to plastic deformation, while B indicates its resistance to fracture. Pugh introduced an index ($B/G = 1.75$) to forecast the ductile (higher B/G) and brittle (lower B/G) behaviors of materials [53]. It is noteworthy that in Table II, the Pugh's B/G ratio value of the $Cs_2PbBeBr_6$ HDP suggested that the material was ductile. This finding is supported by the Poisson's ratio v of 0.247 for the $Cs_2PbBeBr_6$, suggesting that the equilibrium state of this material was ductile. Furthermore, Cauchy's pressure $C_p = C_{12} - C_{44}$ serves to discern the atomic bonding characteristics of materials and provide insights into the bonding type within a compound. A negative C_p value suggests a prevalence of brittle nature, whereas a positive C_p value indicates a ductile nature. In the case of the $Cs_2PbBeBr_6$ HDP, the calculated Cauchy pressure positive, indicating that the $Cs_2PbBeBr_6$ is ductile. This suggests that $Cs_2PbBeBr_6$ demonstrates greater resistance to shearing or deformation caused by shear stress. The stiffness of materials is indeed measured using Young's modulus Y. Materials with a higher Young's modulus value are considered to be stiffer, meaning that they require more force to deform under a given amount of stress. Therefore, Young's modulus serves as a key indicator of a material's stiffness or rigidity. An essential factor to consider in material design is the anisotropy parameter (A), which evaluates whether the physical properties of solids remain consistent in all directions under uniform stress conditions. The value of $A = 1$ indicates isotropic elasticity in the solid, while a material exhibiting elastic anisotropy will have a different A value ($A \neq 1$), indicating a deviation from isotropic elasticity and reflecting the degree of crystallinity distortion. As shown in Table II, the anisotropy factor A is differ than 1, indicating that the $Cs_2PbBeBr_6$ HDP is elastically anisotropic. We determined the melting temperature, denoted as Tm, which is related to the elastic constant through the following equation [54]:

$$T_m = \left(553K + \left[\frac{5.91\,K}{Gpa}\right] \mathrm{C}_{11}\right) \pm 300\ K. \tag{13}$$

The calculated melting temperature of the $Cs_2PbBeBr_6$ HDP is provided in Table II.

3.3. Electronic properties

To evaluate the potential application of $Cs_2PbBeBr_6$ HDP and elucidate its primary optoelectronic properties, we calculated its band structure (BS) and density of states (DOS). Using the optimized structural configuration, we applied the GGA and TB-mBJ potential to compute the BS of $Cs_2PbBeBr_6$ HDP, as shown in Fig. 3. The reason for using the TB-mBJ potential instead of the GGA potential is its enhanced accuracy in predicting electronic band gaps. While the GGA potential tends to underestimate band gaps, especially in semiconductors and insulators, the TB-mBJ potential has been shown to yield more accurate results, often closer to experimental values. This makes it particularly useful for studies focused on electronic properties, where precise band gap predictions are crucial. The band gap value of $Cs_2PbBeBr_6$ HDP is determined using both the GGA and TB-mBJ potentials, as listed in Table III. The calculated indirect band gap values using TB-mBJ and GGA for $Cs_2PbBeBr_6$ HDP are 3.248 eV and 2.243 eV, respectively. TB-mBJ offers a more precise representation of the electronic structure, particularly the band gap, and is recognized for substantially enhancing the band gap values compared to GGA. The $Cs_2PbBeBr_6$ HDP exhibit highly favorable band gaps, making them promising candidates for solar energy harvesting.

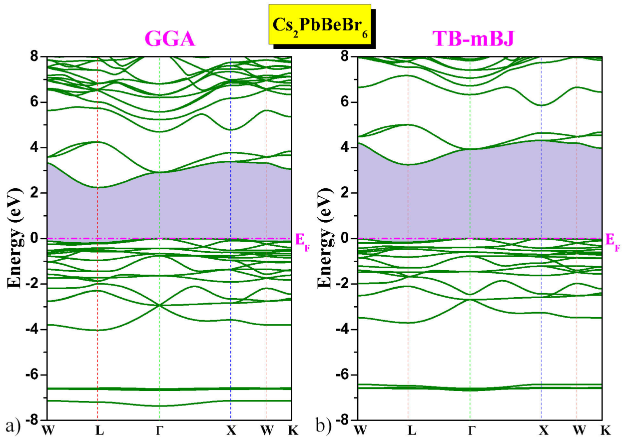

FIGURE 3. Electronic band structure along specific high-symmetry lines in the Brillouin zone, as calculated using the GGA (panel a)) and TB-mBJ (panel b)) for $Cs_2PbBeBr_6$ HDP.

TABLE III. The calculated band gap (E_g, in eV) of the $Cs_2PbBeBr_6$ HDP.

HDP	Method	E_g (eV)
$Cs_2PbBeBr_6$	GGA	2.243 (Γ, X-L)
	TB-mBJ	3.248 (W, Γ, X, K-L)

A deeper understanding of the role played by various energy states in band formation can be achieved by calculating the total density of states (TDOS) and partial density of states (PDOS). Figure 4 displays the TDOS for the valence band and conduction band contributions from Cs, Pb, Be, and Br, as determined by TB-mBJ. The Fermi level is set to 0 eV, as indicated by the vertical dashed lines. The HDP has the highest TDOS peak, as shown in Fig. 4, which roughly falls within the valence band energy range of -6.3 eV to -6.7 eV. The PDOS is also presented in Fig. 4, revealing that the p-Cs and s-Pb states with small peaks of s, p-Be and p-Br states significantly influence valence band generation. On the other hand, the p-Pb states are essential for the development of conduction band, along with minor contributions from the s, p-Be states. This is evident as the p-Br state and unoccupied p-Pb and s, p-Be states shift closer to the Fermi level, playing a crucial role in the optical phenomena. $Cs_2PbBeBr_6$ HDP can be used in various applications due to its specific electronic properties, such as in photovoltaic cells.

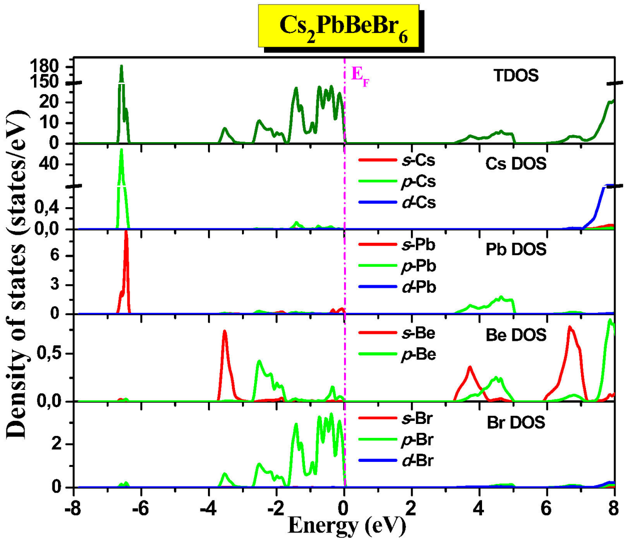

FIGURE 4. Total and partials density of states (TDOS, and PDOS) as calculated using the TB-mBJ for $Cs_2PbBeBr_6$ HDP.

3.4. Optical properties

Understanding optical properties is of great importance across different disciplines in optoelectronic and photovoltaic devices. Therefore, it's essential to accurately measure various optical characteristics, including the reflectance $R(\omega)$, energy loss function $L(\varepsilon)$, absorption $\alpha(\omega)$, refractive index $n(\omega)$, and dielectric function $\varepsilon(\omega)$ as calculated using the TB-mBJ method. The response of materials to light, known as optical sensitivity, is characterized by the complex dielectric function $\varepsilon(\omega)$, expressed as $\varepsilon(\omega) = \varepsilon 1(\omega) + i\varepsilon 2(\omega)$. Here, the real part describes photon dispersion, while the imaginary part signifies photon absorption due to electronic transitions between occupied and unoccupied states [55]. Ambrosch-Draxl and Sofo [56] provide a comprehensive explanation of the methodology employed in the computation of optical properties.

The real component of the dielectric constant, $\varepsilon 1(\omega)$, as depicted in Fig. 5, provides insights into the polarization or dispersion of incident light within the material at plasmonic resonance frequency. The static dielectric function $\varepsilon 1(0)$ values are 3.139 for $Cs_2PbBeBr_6$ HDP, as listed in Table IV. Furthermore, $\varepsilon 1(\omega)$ exhibits a significant increase from the static limit, $\varepsilon 1(0)$, reaching a peak value at the resonance frequency, where ions align to maximize polarization. Then, as the frequency deviates slightly from resonance, the curves decrease to zero values around 10.956 eV. Negative values of $\varepsilon 1(\omega)$ indicate that the material is in a metallic state and reflects all incoming electromagnetic radiation [57-59]. Additionally, the static dielectric constants, $\varepsilon 1(0)$, and the band gap are linked through Penn's model, expressed mathematically as $\varepsilon 1(0) \approx 1 + (\hbar\omega p/Eg)^2$, where Eg represents the optical band gap and ωp signifies the plasma frequency [60]. The observed peaks in the imaginary component $\varepsilon 2(\omega)$ plots are a result of the various potential inter-band transitions within the electronic band structures of $Cs_2PbBeBr_6$ HDP. According to the data in Fig. 5b), the optical band gap of HDP stands around 3.24 eV, identified at the boundary point of $\varepsilon 2(\omega)$, consistent with the electronic band gap. As $\varepsilon 2(\omega)$ values rise from the initial threshold to a peak at 5.075 eV, it predominantly function within the favorable Ultra-Violet (UV) range. This suggests that the investigated $Cs_2PbBeBr_6$ HDP hold significant promise as key candidates for optoelectronic applications.

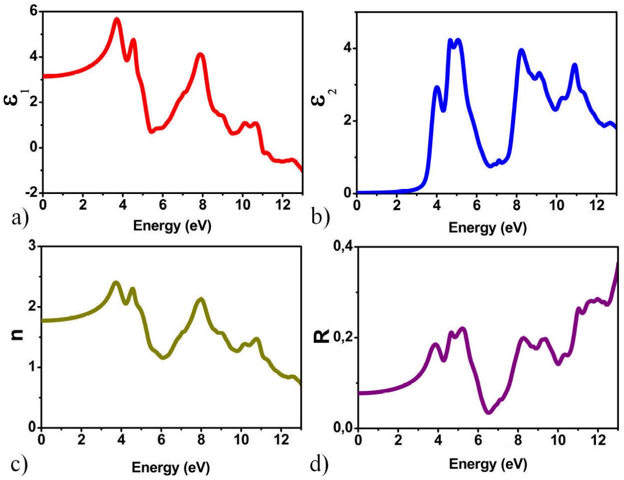

FIGURE 5. Calculated optical parameters a) $\varepsilon 1(\omega)$, b) $\varepsilon 2(\omega)$, c) $n(\omega)$ and d) $R(\omega)$ with photon energy for $Cs_2PbBeBr_6$ HDP.

The refractive index, denoted as $n(\omega)$, holds significance as an optical parameter as it governs the interactions occurring when photon energy interacts with a lattice, revealing the bonding characteristics of materials. This parameter explains the transparency of materials and can be compared with the refractive index of semiconductors [61]. From the data in Fig. 5c), the static refractive index, $n(0)$, are determined to be 1.772 for $Cs_2PbBeBr_6$ HDP. Our findings are supported by the relationship between the static refractive index and dielectric constant, expressed as $n(0)^2 = \varepsilon 1(0)$ [62,63]. Figure 5d) illustrate that the $Cs_2PbBeBr_6$ HDP exhibit it highest reflectivity value of 36.38% (13.0 eV), suggesting its capacity to reflect photons with energies starting from the UV spectra. Additionally, the double perovskite $Cs_2PbBeBr_6$ HDP demonstrates modest reflectivity but notable refractive index values. This make it ideal for incorporation into photovoltaic cells.

The extinction coefficient $k(\omega)$ serves as a metric for measuring the absorption properties of a material in the optical or UV regions of the electromagnetic spectrum. It refers to the rate at which incident light is absorbed over a given

TABLE IV. The calculated static dielectric constant $\varepsilon 1(0)$, static refractive index $n(0)$ and static reflectivity $R(0)$ of $Cs_2PbBeBr_6$ HDP.

HDP	$\varepsilon 1(0)$	$n(0)$	$R(0)$
$Cs_2PbBeBr_6$	3.139	1.172	0.078

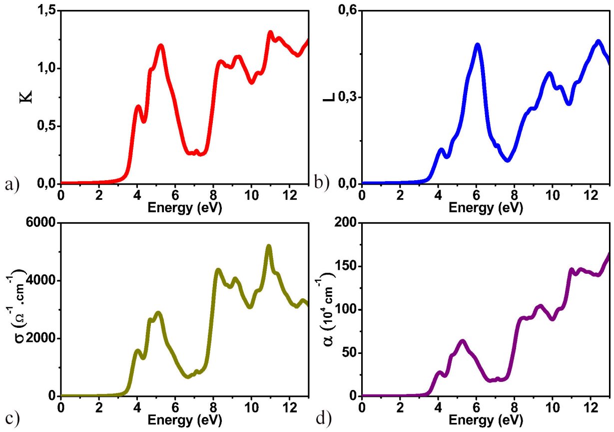

FIGURE 6. Calculated optical parameters a) $K(\omega)$, b) $L(\omega)$, c) $\sigma(\omega)$ and d) $\alpha(\omega)$ with photon energy of $Cs_2PbBeBr_6$ HDP.

distance and is related to the imaginary component of the complex refractive index of the material. The extinction coefficient of $Cs_2PbBeBr_6$ HDP as depicted in Fig. 6a). Specifically, at 0 eV, the peaks of $k(\omega)$ within $Cs_2PbBeBr_6$ HDP correspond to the points where the static extinction coefficient reaches zero. A static extinction coefficient of zero signifies that the material doesn't absorb electromagnetic radiation at a specific wavelength or energy level, indicating high transparency or minimal absorption properties at that particular energy level. The value of the extinction coefficient may vary with the wavelength or frequency of the incident light, thereby illustrating the material's absorption behavior across different segments of the electromagnetic spectrum. From Fig. 6a), it is clear that $Cs_2PbBeBr_6$ HDP has the great intense of the extinction coefficient peak in the UV region. Electron energy loss (EEL) refers to the energy loss of an electron when it interacts with a substance. From Fig. 6b), it's evident that energy loss is minimal within the visible region of the spectrum. It's evident that $Cs_2PbBeBr_6$ HDP exhibits a significant intensity of the $L(\omega)$ peak in the UV region for HDP. Highest electron energy loss refers to the maximum amount of energy that electrons lose when interacting with a material.

The optical conductivity $\sigma(\omega)$ describes the capacity of a material to transmit light, which includes the transitions of electrons between occupied and unoccupied states. Figure 6c) illustrates that $Cs_2PbBeBr_6$ HDP exhibits its highest optical conductivity values at 5208.65 $\Omega^{-1}\text{cm}^{-1}$ (10.898 eV). Highest optical conductivity refers to the maximum level of electrical conductivity exhibited by a material when exposed to electromagnetic radiation. The peak conductivity values of $Cs_2PbBeBr_6$ HDP is predominantly concentrated in the UV region. Figure 6d) reveal that the $Cs_2PbBeBr_6$ HDP exhibits significant absorption $\alpha(\omega)$ peaks in the UV region of the spectrum, indicating a superior energy level. The absorption coefficient values point to an optical band gap of 3.24 eV for $Cs_2PbBeBr_6$ HDP. Additionally, the peaks in the visible region are less intense compared to the ultraviolet region, making them suitable for practical use in ultraviolet optoelectronic devices and photovoltaic cells. Other high-intensity peaks correspond to various electronic transitions. A notable finding is its strong absorption of ultraviolet light, expanding its potential applications, particularly in the advancement of solar cells and other optical devices tailored for the ultraviolet spectrum. A comprehensive study of the optical properties reveals that $Cs_2PbBeBr_6$ HDP is an ideal candidate for optoelectronic applications due to its maximum absorption, minimal reflection, and low optical loss factor in the visible and ultraviolet regions. A comprehensive investigation into the optical properties of $Cs_2PbBeBr_6$ HDP reveals its semiconductors properties.

4. Conclusions

In summary, the structural, elastic, and optoelectronic properties of $Cs_2PbBeBr_6$ HDP were calculated using density functional theory (DFT) with the full-potential linear augmented plane-wave (FP-LAPW) method, as implemented in the Wien2k code. The tolerance factor, the enthalpy of formation, and elastic properties confirm its crystallization in a cubic structure (space group No. 225) and its mechanical stability. The elastic properties also indicate its ductile behavior and anisotropy. Electronic characteristics, computed using the GGA and TB-mBJ methods, revealed indirect band gaps of 2.243 eV and 3.248 eV, respectively. Optical analysis shows that $Cs_2PbBeBr_6$ absorbs energy in the visible and ultraviolet spectra, suggesting its potential for applications in renewable and green energy technologies.

Acknowledgments

This work was financially supported by the Directorate-General for Scientific Research and Technological Development (DGRSDT).

Declarations

Ethical approval

I confirm that this manuscript has not been published elsewhere and is not under consideration by another journal.

Funding

There is no funding for the research.

Data availability

The dataset created and/or analyzed during the current study is available upon reasonable request from the corresponding author.

Contributions

Houda Mansour

Conceptualization, Investigation, Methodology, Data curation, Formal analysis, Software, Writing-original draft, Validation, Visualization. Djamel Rached: Review and editing, Validation, Visualization, Supervision.

Competing interests

The author declares no competing interests.

1. S. H. Shah *et al.*, Comprehensive study of structural, elastic, electronic, optical, and thermoelectric properties of Rb_2NaTlZ (Z = Cl, Br, and I) by DFT, *Mater. Sci. Semicond. Process.* **178** (2024) 108400, `https://doi.org/10.1016/j.mssp.2024.108400`
2. D. Abdullah *et al.*, Probing the opto-electronic, phonon spectrum, and thermoelectric properties of lead-free fluoride perovskites A_2GeSnF_6 (A = K, Rb, Cs) for energy harvesting devices, *Sci. Rep.* **14** (2024) 12644, `https://doi.org/10.1038/s41598-024-61210-3`
3. H. Karwasara *et al.*, A first principle investigations for electronic, optical and mechanical response of novel Ba_2AgIO_6 perovskite, *Phys. Scr.* **98** (2023) 075803, `https://doi.org/10.1088/1402-4896/acdeb5`
4. Z. Zhang *et al.*, Potential Applications of Halide Double Perovskite Cs_2AgInX_6 (X = Cl, Br) in Flexible Optoelectronics: Unusual Effects of Uniaxial Strains, *J. Phys. Chem. Lett.* **10** (2019) 1120, `https://doi.org/10.1021/acs.jpclett.9b00134`
5. S. Al-Qaisi *et al.*, A comprehensive first-principles study on the physical properties of Sr_2ScBiO_6 for low-cost energy technologies, *Opt. Quantum Electron.* **55** (2023) 1015, `https://doi.org/10.1007/s11082-023-05282-x`
6. M. A. Ali *et al.*, Structural, electronic, magnetic and thermoelectric properties of Tl_2NbX_6 (X = Cl, Br) variant perovskites calculated via density functional theory, *J. Comput. Chem.* **44** (2023) 1875, `https://doi.org/10.1002/jcc.27166`
7. S. Thawarkar *et al.*, Experimental and Theoretical Investigation of the Structural and Opto-electronic Properties of Fe-Doped Lead-Free $Cs_2AgBiCl_6$ Double Perovskite, *Chem. Eur. J.* **27** (2021) 7408, `https://doi.org/10.1002/chem.202004902`
8. R. Ullah *et al.*, Effect of cation exchange on structural, electronic, magnetic and transport properties of Ba_2MReO_6 (M = In, Gd), *J. Magn. Magn. Mater.* **546** (2022) 168816, `https://doi.org/10.1016/j.jmmm.2021.168816`
9. Y. Soni *et al.*, Transition metal-based halides double Cs_2ZSbX_6 (Z = Ag, Cu, and X = Cl, Br, I) perovskites: A mechanically stable and highly absorptive materials for photovoltaic devices, *J. Solid State Chem.* **314** (2022) 123420, `https://doi.org/10.1016/j.jssc.2022.123420`
10. A. Bhorde *et al.*, Structural, Electronic, and Optical Properties of Lead-Free Halide Double Perovskite Rb_2AgBiI_6: A Combined Experimental and DFT Study, *ES Mater. Manuf.* **12** (2021) 43, `https://doi.org/10.30919/esmm5f1042`
11. T. Tang *et al.*, First principle comparative study of transitional elements Co, Rh, Ir(III)-based double halide perovskites, *Mater. Today Commun.* **34** (2023) 105431, `https://doi.org/10.1016/j.mtcomm.2023.105431`
12. Y. Chrafih *et al.*, Thermodynamic, optical, and morphological studies of the Cs_2AgBiX_6 double perovskites (X = Cl, Br, and I): Insights from DFT study, *J. Alloys Compd.* **960** (2023) 170650, `https://doi.org/10.1016/j.jallcom.2023.170650`
13. G. Nazir *et al.*, Tuning of band gap by anions (Cl, Br, I) of double perovskites Rb_2AgAsX_6 for solar cells and thermoelectric applications, *Phys. Scr.* **98** (2023) 025811, `https://doi.org/10.1088/1402-4896/acaec1`
14. M. Z. Kazim *et al.*, Physical properties of Ba_2XIO_6 (X = Ag, Na) double perovskite oxides for energy harvesting devices, *Arab. J. Sci. Eng.* **48** (2022) 779, `https://doi.org/10.1007/s13369-022-06985-1`
15. E. Haque *et al.*, Electronic, phonon transport and thermoelectric properties of $Cs_2InAgCl_6$ from first-principles study, *Comput. Condens. Matter* **19** (2019) e00374, `https://doi.org/10.1016/j.cocom.2019.e00374`
16. T. Ishibe *et al.*, Methodology of Thermoelectric Power Factor Enhancement by Controlling Nanowire Interface, *ACS Appl. Mater. Interfaces.* **10** (2018) 37709, `https://doi.org/10.1021/acsami.8b13528`
17. L. Peedikakkandy *et al.*, Lead free, air stable perovskite derivative Cs_2SnI_6 as HTM in DSSCs employing TiO_2 nanotubes as photoanode, *Mater. Res. Bull.* **108** (2018) 113, `https://doi.org/10.1016/j.materresbull.2018.08.046`
18. E. Haque *et al.*, Origin of ultra-low lattice thermal conductivity in Cs_2BiAgX_6 (X = Cl, Br) and its impact on thermoelectric performance, *J. Alloys Compd.* **748** (2018) 63, `https://doi.org/10.1016/j.jallcom.2018.03.137`
19. M. A. Green *et al.*, The emergence of perovskite solar cells, Nat. Photonics **8** (2014) 506, `https://doi.org/10.1038/nphoton.2014.134`
20. L. Zhou *et al.*, Synthesis and Photocatalytic Application of Stable Lead-Free $Cs_2AgBiBr_6$ Perovskite Nanocrystals, *Small.* **14** (2018) 1703762, `https://doi.org/10.1002/smll.201703762`
21. S. A. Aldaghfag *et al.*, Computational study of Cs_2ScXBr_6 (X=Ag, Tl) for renewable energy devices, *Physica B.* **646** (2022) 414277, `https://doi.org/10.1016/j.physb.2022.414277`
22. M. Caid *et al.*, Comprehensive exploration of halide double perovskites Cs_2B[2B9?]$GeCl_6$ (B[2B9?]: Zn, Cd) for affordable energy technologies: a high-throughput investigation, *Opt.*

Quantum Electron. **56** (2024) 980, https://doi.org/10.1007/s11082-024-06721-z

23. N. Shrivastav *et al.*, Predicting photovoltaic efficiency in Cs-based perovskite solar cells: A comprehensive study integrating SCAPS simulation and machine learning models, Solid state Commun. **380** (2024) 115437, https://doi.org/10.1016/j.ssc.2024.115437
24. M. Grätzel, The light and shade of perovskite solar cells, *Nat. Mater*. **13** (2014) 838, https://doi.org/10.1038/nmat4065
25. A. T. Barrows *et al*., Efficient planar heterojunction mixed-halide perovskite solar cells deposited via spray-deposition, *Energy Environ. Sci*. **7** (2014) 2944, https://doi.org/10.1039/c4ee01546k
26. S. Al-Qaisi *et al*., First-principles investigations of Ba_2NaIO_6 double Perovskite semiconductor: Material for low-cost energy technologies, *Mater. Chem. Phys*. **275** (2022) 125237, https://doi.org/10.1016/j.matchemphys.2021.125237
27. A. K. Jena *et al*., Halide Perovskite Photovoltaics: Background, Status, and Future Prospects, *Chem. Rev.* **119** (2019) 3036, https://doi.org/10.1021/acs.chemrev.8b00539
28. M. Caid *et al*., A Density Functional Theory Exploration of Cs_2B[2032?]B[2033?]I_6 (B[2032?]B[2033?]: BeCa, BeSr, GeCd, GeBe, GeMg) Halide Double Perovskites for Optimal Solar Cell and Renewable Energy Applications, *Phys. Status Solidi B.* **261** (2024) 2300577, https://doi.org/10.1002/pssb.202300577
29. M. Caid *et al*., Structural, elastic, electronic, and optical properties of lead-free halide double perovskites Cs_2 B’ B” Br_6 (B’B”: BeMg, CdBe, CdGe, GeMg, GeZn, MgZn): Ab initio calculations, *J. Mol. Model*. **30** (2024) 59, https://doi.org/10.1007/s00894-024-05861-z
30. M. Caid *et al*., Exploring the versatile properties of $Cs_2B'GeF_6$ (B': Sn, Pb) double perovskites: Insights into their mechanical stability, optoelectronic potential, and high thermoelectric performance, *Physica B.* **677** (2024) 415742, https://doi.org/10.1016/j.physb.2024.415742
31. M. Caid *et al.*, Theoretical insight of stabilities and optoelectronic properties of double perovskite Cs_2CuIrF_6: Ab-initio calculations, *J. Mol. Model*. **29** (2023) 178, https://doi.org/10.1007/s00894-023-05588-3
32. M. Caid *et al.*, DFT calculations on physical properties of the lead-free halide-based double perovskite compound $Cs_2CdZnCl_6$, Solid State Commun. **369** (2023) 115216, https://doi.org/10.1016/j.ssc.2023.115216
33. D. Y. Hu *et al.*, First-principles study on the structural, elastic, electronic and optical properties of lead-free double perovskites Cs_2CuBiX_6 (X: I, Br, Cl), *Mater. Today Commun*. **29** (2021) 102842, https://doi.org/10.1016/j.mtcomm.2021.102842
34. M. Saeed *et al.*, Optoelectronic and elastic properties of metal halides double perovskites Cs_2InBiX_6 (X = F, Cl, Br, I), *Chin. Opt. Lett.* **19** (2021) 030004, https://doi.org/10.3788/col202119.030004
35. P. Blaha *et al*., Full-potential, linearized augmented plane wave programs for crystalline systems, *Comput. Phys. Commun*. **59** (1990) 399, https://doi.org/10.1016/0010-4655(90)90187-6
36. J. P. Perdew *et al.*, Generalized Gradient Approximation Made Simple, *Phys. Rev. Lett.* **77** (1996) 3865, https://doi.org/10.1103/physrevlett.77.3865
37. F. Tran *et al*., (2009) Accurate Band Gaps of Semiconductors and Insulators with a Semilocal Exchange-Correlation Potential, *Phys. Rev. Lett*. **102** (2009), https://doi.org/10.1103/physrevlett.102.226401
38. F. D. Murnaghan, The Compressibility of Media under Extreme Pressures, *Proc. Natl. Acad. Sci. U.S.A.* **30** (1944) 244, https://doi.org/10.1073/pnas.30.9.244
39. Z. Li *et al*., Stabilizing Perovskite Structures by Tuning Tolerance Factor: Formation of Formamidinium and Cesium Lead Iodide Solid-State Alloys, *Chem. Mater*. **28** (2015) 284, https://doi.org/10.1021/acs.chemmater.5b04107
40. S. A. Khandy *et al*., Analysing cation-modified magnetic perovskites A_2SnFeO_6 (A = Ca, Ba): a DFT study, *RSC Adv*. **11** (2021) 27499, https://doi.org/10.1039/d1ra03527d
41. M. Caid et al., First principles study of the structural, elastic, magneto-electronic and thermoelectric properties of double perovskite Ba_2ZrFeO_6 in ferrimagnetic phase, *Comput. Condens. Matter*. **37** (2023) e00847, https://doi.org/10.1016/j.cocom.2023.e00847
42. R. Hill, The Elastic Behaviour of a Crystalline Aggregate, *Proc. Phys. Soc. A.* **65** (1954) 349, https://doi.org/10.1088/0370-1298/65/5/307
43. M. Jamal *et al*., Elastic constants of cubic crystals, *Comput. Mater. Sci*. **95** (2014) 592, https://doi.org/10.1016/j.commatsci.2014.08.027
44. M. Born *et al*., Dynamical Theory of Crystal Lattices, Clarendon Press, (Oxford, 1954), https://doi.org/10.1119/1.1934059
45. D. G. Pettifor, Theoretical predictions of structure and related properties of intermetallics, *Mater. Sci. Technol.* **8** (1992) 345, https://doi.org/10.1179/mst.1992.8.4.345
46. W. Voigt, Ueber die Beziehung zwischen den beiden Elasticitätsconstanten isotroper KÃ¶rper, *Ann. Phys.* **274** (1889) 573, https://doi.org/10.1002/andp.18892741206
47. A. Reuss, B. der Fließgrenze von M. auf Grund der P. für Einkristalle, *Z. Angew. Math. Mech*. **9** (1929) 49, https://doi.org/10.1002/zamm.19290090104
48. J. F. Nye *et al*., Physical Properties of Crystals: Their Representation by Tensors and Matrices, *Phys. Today.* **10** (1957) 26, https://doi.org/10.1063/1.3060200
49. H. Fu *et al*., Ab initio calculations of elastic constants and thermodynamic properties of NiAl under high pressures, *Comput. Mater. Sci*. **44** (2008) 774, https://doi.org/10.1016/j.commatsci.2008.05.026
50. M. Friák *et al*., Ab initio calculation of tensile strength in iron, *Philos. Mag.* **83** (2003) 3529, https://doi.org/10.1080/14786430310001605588

51. Y. Pan *et al.*, Ab-initio investigation of structure and mechanical properties of PtAlTM ternary alloy, *Vacuum.* **151** (2018) 205, `https://doi.org/10.1016/j.vacuum.2018.02.027`
52. L. Hao *et al.*, Ab Initio Study of the Structural, Electronic, Magnetic, Mechanical and Thermodynamic Properties of Full-Heusler Mn_2CoGa, *J. Electron. Mater*. **48** (2019) 6222, `https://doi.org/10.1007/s11664-019-07417-x`
53. S. F. Pugh, XCII. Relations between the elastic moduli and the plastic properties of polycrystalline pure metals, *Philos. Mag.* **45** (1954) 823, `https://doi.org/10.1080/14786440808520496`
54. I. E. Rabah *et al*., A Theoretical Analysis of Physical Properties and Half-Metallic Stability under Pressure Effect of the ScNiCrZ (Z=Ga, Al, In) Heusler Alloys, *SPIN*. **11** (2021) 2150007, `https://doi.org/10.1142/s2010324721500077`
55. M. Caid *et al.*, Electronic structure of short-period ZnSe/ZnTe superlattices based on DFT calculations, *Condens. Matter Phys*. **25** (2022) 13701, `https://doi.org/10.5488/cmp.25.13701`
56. C. Ambrosch-Draxl e*t al*., Linear optical properties of solids within the full-potential linearized augmented planewave method, *Comput. Phys. Commun*. **175** (2006) 1, `https://doi.org/10.1016/j.cpc.2006.03.005`
57. Y. Rached *et al*., Effects of stacking periodicity on the structural, electronic, optical and thermoelectric properties of GaSb/InSb superlattices, *Mater. Sci. Semicond. Process.* **156** (2023) 107297, `https://doi.org/10.1016/j.mssp.2022.107297`
58. H. Mancer *et al*., Probing the effect of different exchange-correlation functionals on the optoelectronic features of chalcogenide compound Ag_2O, *Rev. Mex. Fis*. **69** (2023) 011004 1, `https://doi.org/10.31349/revmexfis.69.011004`
59. M. Caid *et al.*, Full potential study of the structural, electronic and optical properties of $(InAs)_m/(GaSb)_n$ superlattices, *Comput. Condens. Matter* **21** (2019) e00394. `https://doi.org/10.1016/j.cocom.2019.e00394`
60. D. R. Penn, Wave-Number-Dependent Dielectric Function of Semiconductors, *Phys. Rev.* **128** (1962) 2093, `https://doi.org/10.1103/physrev.128.2093`
61. M. Caid *et al.*, Investigation of structural, elastic, electronic, and optical properties of lead-free double perovskites Cs_2XBeBr_6 (X = Ge, Sn): a first-principles DFT study, *J. Mol. Model.* **30** (2024) 354, `https://doi.org/10.1007/s00894-024-06158-x`
62. S. Morsli *et al*., Electronic structure and optoelectronic behavior of $MgPbP_2$ chalcopyrite, *Comput. Condens. Matter*. **27** (2021) e00550, `https://doi.org/10.1016/j.cocom.2021.e00550`
63. M. Caid et al., High-throughput study of the structural, electronic, and optical properties of short-period (BeSe)m/(ZnSe)n superlattices based on DFT calculations, *Comput. Condens. Matter.* **29** (2021) e00598, `https://doi.org/10.1016/j.cocom.2021.e00598`